[AMERICAN JOURNAL OF SCIENCE, VOL. 277, OCTOBER, 1977, P. 913-936]

American Journal of Science

GL03759

OCTOBER 1977

TRANSPORT PHENOMENA IN HYDROTHERMAL SYSTEMS: THE NATURE OF POROSITY

D. NORTON and R. KNAPP

Department of Geosciences,
University of Arizona, Tucson, Arizona 85721

ABSTRACT. Porosity of rocks may be described by $\phi_{Total} = \phi_{Flow} + \phi_{Diffusion} + \phi_{Residual}$. Laboratory experiments indicate that total porosities of fractured rocks in hydrothermal systems range from 0.2 to 0.01, and diffusion porosities range from 10^{-3} to 10^{-6}. Synthesis of data from the literature and field observations of fracture characteristics indicate that flow porosities range from 10^{-3} to 10^{-6}. Therefore, the major portion of total porosity in pluton environments is due to residual pores not interconnected to either flow or diffusion porosity.

Permeability may be defined as a function of the abundance and geometry of continuous flow channels. Our observations suggest that a planar fracture model is a reasonable first order approximation for fractures in pluton environments. An analysis of aperture, abundance, and continuity indicates permeabilities on the order of 10^{-14} cm^2 may characterize large regions of the crust.

The proposed porosity model affords for the definition of the interface between circulating hydrothermal fluids and reactant minerals in a manner consistent with the physical phenomena and with the partial differential equations that describe advection-diffusion-reaction processes.

NOTATION

- A — area (cm^2)
- A_i — volumetric source of i^{th} component
- b — half the fracture aperture (cm)
- B — coordinate of fracture aperture (cm)
- d — fracture aperture (cm)
- D_{ik} — diffusion coefficient of the i^{th} ion due to a concentration gradient of the k^{th} ion (kgH_2O cm^{-1} sec^{-1})
- f — fracture frequency (cm fracture^{-1})
- F_D — fluid driving force (g cm sec^{-2})
- F_r — fluid resistive force (g cm sec^{-2})
- k — permeability (cm^2)
- l — unit length (cm)
- m_i — molality of the i^{th} component (moles kgH_2O^{-1})
- M_i — moles of the i^{th} component
- n — fracture abundance (fractures cm^{-1})
- Q — volumetric flow rate (cm^3 sec^{-1})
- S — surface area (cm^2)
- $\bar{S}_i$ — summation of component fluxes for the i^{th} ion (mols cm^{-2} sec^{-1})
- t — time (sec)
- $\bar{u}_i$ — flux of the i^{th} component (moles cm^{-2} sec^{-1})

$\bar{v}$ — fluid velocity (cm sec^{-1})
V — representative elemental volume (cm^3)
δ_c — width of concentration boundary layer (cm)
δ_o — width of laminar flow profile (cm)
η — viscosity (g cm^{-1} sec^{-1})
ν — viscosity (cm^2 sec^{-1})
ρ — fluid density (g cm^{-3})
ρ_β — bulk density (g cm^{-3})
ρ_γ — grain density (g cm^{-3})
σ — shear stress (g cm^{-1} sec^{-2})
τ — tortuosity of pores
ϕ_D — total diffusion porosity
ϕ_F — flow porosity
ϕ_R — residual porosity
ϕ_T — total porosity
ϕ'_D — equal to the directional diffusion porosity divided by τ
$\bar{\phi}$ — equal to ϕ'_D/ϕ_D
Ω — fluid potential (g cm^{-1} sec^{-2})
∇ — operator, $\frac{\partial}{\partial x} + \frac{\partial}{\partial y} + \frac{\partial}{\partial z}$ (cm^{-1})

INTRODUCTION

The interface between circulating aqueous solutions and reactant mineral phases is defined by the relative distribution of solution filled pores and minerals. This interface is a controlling factor in the chemical mass transfer that typically occurs between minerals and solutions in geochemical systems. Conceptual models that have been developed for the sedimentary rock environment (Fatt, 1956) neither adequately describe low total porosity and systematically developed fractures characteristic of igneous rocks nor do they account for the distribution of alteration minerals found in hydrothermal systems. Alteration minerals in hydrothermal systems occur both along and adjacent to continuous fractures. The compositions and assemblages of these minerals do not change over distances of meters to hundreds of meters parallel to the fractures, whereas abrupt changes occur normal to the fracture plane over distances of only millimeters to tens of centimeters. In rocks where the fracture sets are sufficiently close-spaced, the alteration zones may overlap, thereby producing a continuous zone of alteration products normal to the adjacent fractures. These aspects of mineral distributions suggest that the two principal modes of aqueous ion transport are by fluid flow along fractures and by aqueous diffusion away from the fractures.

The reaction between circulating fluids and their host rocks and the diffusion of aqueous ions to and away from flow channels may be described in terms of partial differential equations. Since the distribution of alteration mineral products predicted by the numerical solution to

these equations depends directly on the nature of porosity, the following porosity model was developed.

Porosity model.—The total porosity in fractured media, ϕ_T, may be represented by

$$\phi_T = \phi_F + \phi_D + \phi_R; \tag{1}$$

ϕ_F is the effective flow porosity and represents those pores through which the dominant mode of fluid and aqueous species transport is by fluid flow; ϕ_D is the diffusion porosity and represents those pores through which the dominant mode of transport is by diffusion through the aqueous phase (Garrels, Dreyer, and Howland, 1949); ϕ_R is the residual porosity and represents those pores not connected to ϕ_F or ϕ_D. The geometry and distribution of these pore types is apparent in many outcrops (pl. 1) where one can readily observe continuous fracture sets, ϕ_F, and less continuous sets, ϕ_D. These field observations, together with laboratory measurements that define total diffusion and residual porosity, suggest the porosity distribution in these types of outcrops can be schematically represented by figure 1.

TOTAL POROSITY

The total porosity of a rock is defined by

$$\phi_T = 1 - \frac{\rho_\beta}{\rho_\gamma} \tag{2}$$

where ρ_β is the dry rock bulk density of a representative sample determined by standard immersion techniques, and ρ_γ is the grain density, determined on a finely ground sample with a grain size less than the minimum pore diameter. The porosity determined in this manner is a measure of the total pore volume in rock, if the sample represents all porosity types. Partial or total saturation of the pores with fluid would introduce errors on the order of 2 percent of the total porosity for rocks in the ≤ 0.05 porosity range.

FLOW POROSITY

The flow porosity of fractured rocks is that portion of the total rock that constitutes rock permeability. Continuous pore features in pluton environments include planar features such as faults, joints, cracks, or bedding planes in layered host rocks. A simple flow porosity model based on open-smooth-walled fractures appears to be a reasonable first approximation of permeability.

Fluid flow in natural systems is characterized by laminar flow (fig. 2), which is the basis for development of equations that relate fracture characteristics to rock permeability. Following the formulations of DeWeist (1969), Snow (ms, 1970), and Maini (ms), a representative elemental volume, V, is chosen such that it contains a single fracture parallel to the x-y coordinate axis. A functional expression is derived for one-dimensional fluid velocity at any point in the fracture cross section from

PLATE 1

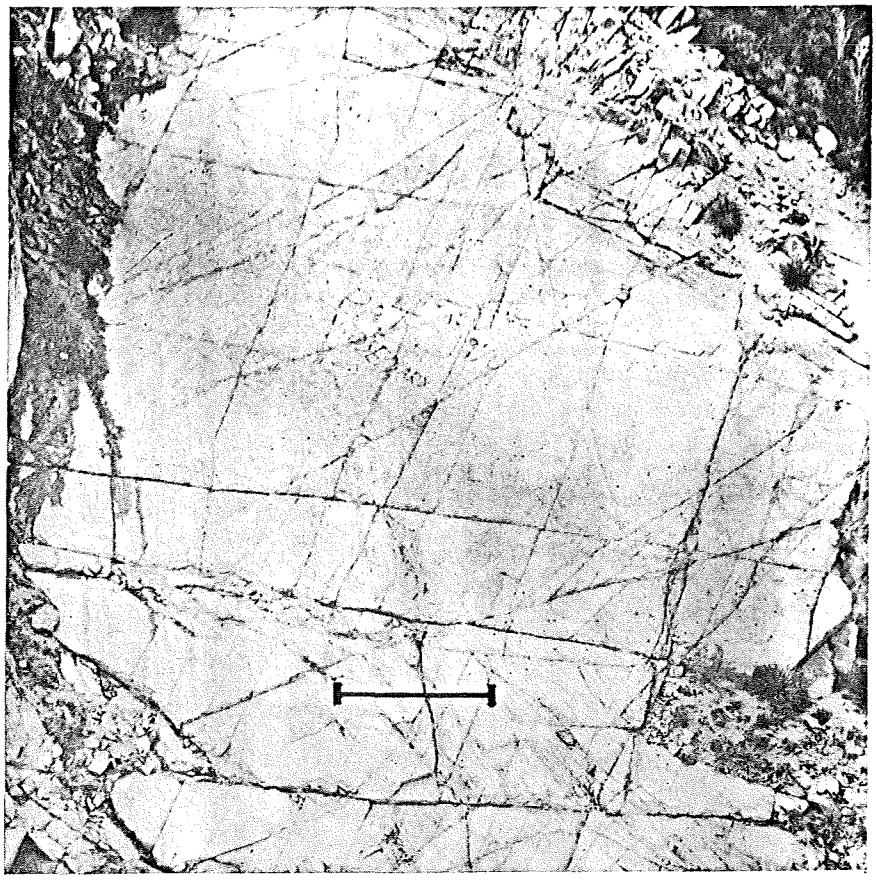

Outcrop of the porphyritic Schultze Granite demonstrating the geometry and distribution of flow and diffusion porosity. Continuous fractures, which cross cut outcrop, represent flow channels, and discontinuous fractures represent diffusion porosity. Scale bar is 5 m.

the differential equation describing the flow. This function is then used to find the mass flow along the fracture by integrating the velocity function over the fracture opening.

Steady state flow conditions require equality between the fluid driving force, F_d, and the resistive viscous force, F_r. The driving force is determined by the gradient in fluid potential and the area on which the force acts:

$$F_d = lA\nabla\Omega. \tag{3}$$

The resistive force is due to shear stress acting on the surface area, S, of the fracture walls:

$$F_r = \sigma S. \tag{4}$$

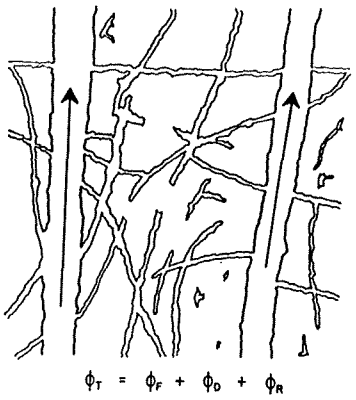

Fig. 1

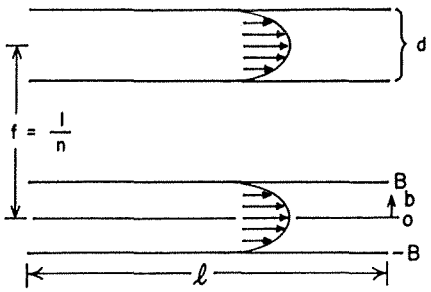

Fig. 2

Fig. 1. Schematic representation of constituent porosities showing the geometric relationships between residual pores, ϕ_R, diffusion pores, ϕ_D, and flow pores, ϕ_F. The arrows denote an arbitrarily chosen direction of fluid flow in ϕ_F. The pores extending from these two flow channels either have apertures that are too small to permit significant fluid flow or are discontinuous; therefore, all these pores are ϕ_D. The relative abundances are not shown.

Fig. 2. The laminar flow profile in planar fractures due to viscous drag forces at the walls. f is the fracture spacing and d the aperture. B and −B represent the limits of integration in eq (9).

where $S = 2l$, and l is the unit length of the representative elemental volume. The shear stress in a viscous fluid is related to the fluid velocity by:

$$\sigma = -\eta \frac{d\bar{v}}{db}, \tag{5}$$

where $b = \frac{1}{2}$ fracture aperture (cm). The area on which the fluid driving force acts is orthogonal to the direction of flow in the fracture:

$$A = 2b \tag{6}$$

Combining eqs (3-6), we have a differential equation in terms of fluid velocity and distance from the fracture wall:

$$d\bar{v} = -b \frac{\nabla\Omega}{\eta} db. \tag{7}$$

Integrating eq (7) and evaluating the integration constant by using $\bar{v} = 0$ when $b = B$ gives the velocity profile across the aperture of a single fracture:

$$\bar{v} = \frac{\nabla\Omega}{2\eta}(B^2 - b^2). \tag{8}$$

This parabolic flow profile develops in less than 1 m along the fracture for fluid velocities less than 10 cm/sec, and we will, therefore, assume in subsequent discussions that this flow profile is fully developed in geologic systems.

The volumetric flow rate from a single fracture is defined by first considering the flow velocity through an incremental cross-sectional area of the fracture and then integrating this expression over the fracture opening orthogonal to the flow direction (fig. 2).

$$Q = \int_{-B}^{B} \frac{l \nabla \Omega}{2\eta} (B^2 - b^2)\, db. \tag{9}$$

Integrating eq (9) gives the flow rate,

$$Q = \frac{-2B^3 \nabla \Omega}{3\eta} \tag{10}$$

per unit length, l, of a single fracture. Substituting the aperture of the fracture into (10) gives the volume flow rate from n such parallel fractures

$$Q = \frac{-nd^3 \nabla \Omega}{12\eta}. \tag{11}$$

The general statement of Darcy's Law for flow through porous media is (Hubbert, 1940):

$$Q = \frac{-k \nabla \Omega}{\eta}, \tag{12}$$

and k is a factor describing the shape and length characteristics of the flow passages. By analogy of (12) to (11) we see this intrinsic rock parameter, permeability, for fracture controlled flow is:

$$k = \frac{nd^3}{12}. \tag{13}$$

Fracture sets in natural systems are not precisely represented by this model; however, anisotropic characteristics of the fractures may be formulated into a tensor form:

$$Q = -\frac{k_{ij}}{\eta} \nabla \Omega, \tag{14}$$

where k_{ij} is the permeability tensor in which the subscript i relates to the fluid flow direction, and j relates to the potential gradient direction.

The porosity of the flow channels is also related to the fracture aperture and abundance, where

$$\phi_F = nd \tag{15}$$

for a single parallel fracture set.

Field observations of abundance and aperture on parallel fracture sets, together with eq (13), permit permeability estimates to be made. Abundances of fractures in plutons vary from 0.5 fracture/cm in some ore deposits (Bingham, Utah) to 10^{-3} fractures/cm in unaltered igneous bodies (Villas, ms; Bianchi and Snow, 1969). Aperture variations, which

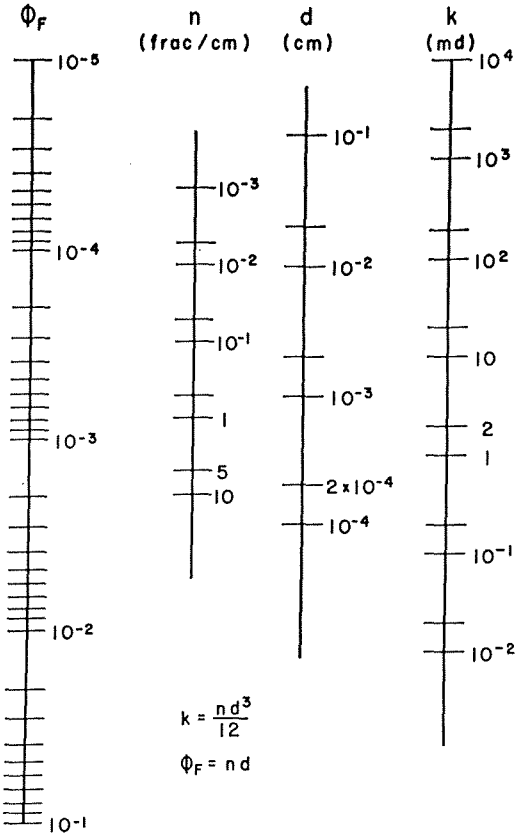

Fig. 3. Graphical solution to eqs (13) and (15). Aperture estimates, d, range from 5×10^{-6} to 2×10^{-2} cm, whereas fracture abundances, n, range from 5×10^{-1} to 10^{-3}/cm. With $d = 10^{-4}$ cm and $n = 5 \times 10^{-1}$/cm, $\phi_F = 5 \times 10^{-5}$ and $k = 4 \times 10^{-8}$ md where 10^{-11} cm^2 = 1 millidarcy.

have the greatest effect on permeability but are the least well known, may range from 5×10^{-5} to 2×10^{-2} cm. Though these ranges in apertures and abundances are large, they place some interesting constraints on the magnitude of flow porosity when examined with respect to a single fracture set, compare eqs 13 and 15 and their graphical solution (fig. 3). The maximum range in flow porosity is from 10^{-2} to 5×10^{-8}. Values estimated by Villas (ms) on the Mayflower Pluton range from 2×10^{-3} to 3×10^{-5}. The comparable total porosities for the Mayflower diorite are in the range of 0.01 to 0.03. Similarly, the flow porosity and the total porosity of the Sherman Granite are 5×10^{-6} and 10^{-2}, respectively (Pratt and others, 1974). We, therefore, conclude that the flow porosities are generally a small fraction of the total porosities, even though precise limits can not be established.

Measurements of permeability by different methods often yield significantly different values. In general, in-situ measurements of permea-

bility on large representative blocks of fractured rock indicate values in the range of 10^{-12} to 10^{-8} cm^2 (table 1). An in-situ experiment conducted on the Sherman Granite determined the permeability of this rock to be 10^{-11} cm^2, whereas the permeability determined on intact core samples is about 2 to 3 orders of magnitude lower. Laboratory measurements of intact core samples of limestones, dolomites, and granites (table 1) also indicate very low values of permeability. Clearly, the permeability of rocks in hydrothermal systems is a poorly known quantity.

Estimates of rock permeabilities in the Earth's crust rely on deep drill holes, 10 km in sedimentary basins and 4 to 5 km in crystalline rocks, abundance and aperture of continuous fractures, electrical resistivity profiles, elastic properties of intact rock samples, and seismic data. These various lines of indirect evidence suggest that permeabilities to depths of 10 to 15 km may be significantly greater than 10^{-14} cm^2. Whereas laboratory measurements indicate that a pressure increase from 1 bar to 1 kb produces a $10^{1.5}$ decrease in permeability (Brace, Walsh, and Frangos, 1968), seismic hypocentral data suggest that brittle rock failure and transient fractures occur at depths to at least 15 to 20 km. The persistence of continuous fractures filled with conductive pore fluids at considerable depths is further indicated by relatively high electrical conductivities in the middle to upper crust (Plauff, 1966; Jackson, 1966; Keller, Anderson, and Pritchard, 1966; and Brace, 1971).

The permeability of fractured crystalline rocks is due to continuous fractures, and, even though the rock mass between these channels has a

TABLE 1

Some permeability measurements on crystalline rocks

Rock type	k(cm^2)	ϕ_F	Method	Reference
Hardhat-granite	10^{-9}-10^{-12}		pump	Boardman and Skrove, 1966
Sherman-granite	10^{-11}	2×10^{-5}	pump	Pratt and others, 1974
Sherman-granite	$< 10^{-14}$		core	Pratt and others, 1974
Quartz porphyry	$\backsim 10^{-11}$		pump	Cadek and others, 1968
Gneiss-schist	5×10^{-11}		pump test in fractured zone	Marine, 1966
Gneiss-schist	5×10^{-14}		pump (without fractures)	Marine, 1966
Gneiss-schist	10^{-15}		core	Marine, 1966
Metabasalt	2×10^{-8}		pump	Davis, 1969
Schist	1.4×10^{-8}		pump	Davis, 1969
Quartz diorite	10^{-7} to 3×10^{-10}	2×10^{-3} to 3×10^{-3}	planar fracture model	Villas, ms.
Granite	10^{-4} to 10^{-10}	5×10^{-2} to 4×10^{-5}	planar fracture model	Bianchi and Snow, 1969
Welded tuff	$< 2\times10^{-16}$		pump	Winograd, 1971
Bedded tuff	10^{-10}-10^{-12}		pump	Winograd, 1971
Granite	10^{-14}-10^{-17}		core*	Brace, Walsh, and Frangos, 1968
Limestone	2×10^{-15}		disk	Ohle, 1951
Dolomite	10^{-10}		disk	Ohle, 1951
Volcanic (clastics)	10^{-8}-6×10^{-12}		drawn down	Grindley, 1965

* Measured as a function of effective pressure

relatively high total porosity, its effective permeability is nil. This fact is also evidenced by the above observations and the distribution of hydrothermal alteration minerals along the walls of fractures. The fact that alteration minerals occur in veins in ore deposits and active geothermal systems clearly demonstrates the nature of fracture controlled fluid flow. The widespread chemical alteration of rocks in hydrothermal systems further attests to the relatively large permeability of rocks in the Earth's crust.

The importance of deducing broad scale permeabilities of the crust relates directly to studies of the mass movement of aqueous solutions in the crust. Permeabilities greater than 10^{-14} cm^2 are conducive to the circulation of fluids in pluton environments and perhaps over broader regions of the crust (Norton and Knight, 1977). Also, since flow porosity in fractured igneous rocks, and possibly in fractured rocks in general, is apparently a small fraction of the total rock porosity, 10^{-1} to 10^{-5}, the true velocity of particles within a flow fracture, eq (8), will be orders of magnitude greater than the superficial velocity.

$$\bar{v}_{true} = \frac{\bar{v}_{Darcy}}{\phi_F} \tag{16}$$

DIFFUSION POROSITY

The nature of diffusion porosity is apparent, if we consider a typical region, R, within which the transport of aqueous components by fluid flow is insignificant with respect to diffusional transport. These conditions may occur in regions characterized by discontinuous fractures, small aperture fractures, or discontinuous pores. This type of region is typically bounded by continuous sets of fractures which constitute the flow channels in the overall system (fig. 1).

The diffusional flux of the i^{th} ion from the region is defined by the flux vector normal to an incremental area of the region's surface, S,

$$\bar{u}_i = -\phi'_D \sum_k D_{ik} \nabla m_k \tag{17}$$

where ϕ'_D is the ratio of the diffusion porosity coincident with the normal flux vector to the tortuosity, τ, of the pores, m_k is the concentration of the k^{th} ion in molality, and D_{ik} is the diffusion coefficient of the i^{th} ion due to the gradient in concentration of the k^{th} ion. The amount of the i^{th} ion leaving the region, with respect to the volume, is given by the volume integral of the divergence of $\bar{u}_i$,

$$\frac{\partial M_i}{\partial t} = \int_R \text{div } \bar{u}_i dV, \tag{18}$$

whereas the change in the amount of the i^{th} aqueous ion contained within the region as a function of time, is given by,

$$\frac{\partial M_i}{\partial t} = \int_R \rho \phi_D (1 + A_i) \frac{\partial m_i}{\partial t} dV, \tag{19}$$

where ϕ_D is the total diffusion porosity, and A_i is a volumetric source or sink of the i^{th} ion which, in effect, describes the irreversible mass transfer between the aqueous and solid phases. The amount leaving and amount depleted must be equal; therefore, eqs (18) and (19) are equal. Since the integrals hold for any subregion in R, the integrals can be eliminated. Eqs (18) and (19) are combined to describe the conservation of the i^{th} aqueous species in R:

$$\rho\phi_D (1 + A_i) \frac{\partial m_i}{\partial t} = \nabla \cdot \phi'_D \sum_k D_{ik} \nabla m_k. \tag{20}$$

The magnitude and distribution of the directional diffusion porosity, ϕ'_D, as defined by eq (17), have been measured on a variety of rocks. The total diffusion porosity is determined by experiments where $A_i = 0$ and $k = 1$ and are calculated by rearranging (20).

$$\frac{\partial m_i}{\partial t} = \rho D_i \bar{\phi} \nabla^2 m_i, \tag{21}$$

where

$$\bar{\phi} = \frac{\phi'_D}{\phi_D} \tag{22}$$

Eq (21) is then solved numerically to yield $\bar{\phi}$, which substituted in eq (22) gives ϕ_D.

Experimental apparatus modified from Garrels, Dreyer, and Howland (1949) was used to obtain the diffusion porosity data (Knapp, ms). Rock wafers, 1.0 to 2.5 cm in radius and from about 0.2 to 1.0 cm thick, are embedded with epoxy in Plexiglas plugs, so that only the circular surfaces are exposed. The samples are then saturated by drawing 10^{-4} N KCl solution through the wafer for at least 24 hrs. Microscopic examination of the wafers serves to check the epoxy seal for leakage and the rock for any induced fractures.

The plug with the saturated rock is next placed in a Plexiglas diffusion cell; the cell is filled with a measured amount (usually 60 ml) of 10^{-4} N KCl solution, and electrodes are inserted into the cell. The entire assemblage is placed in a thermally insulated, 25°C, tank containing about 10 l of 1 N KCl solution, which sets up an activity gradient across the rock wafer. Care is taken to minimize any fluid potential gradient between the cell and the tank to a negligible value. The concentration change is monitored by conductometric methods.

The experimental error in these measurements is difficult to define precisely. But, based on ϕ'_D measured on adjacent samples of apparently homogeneous and isotropic rocks, the precision is between 4 and 30 percent (Knapp, ms). Though this upper limit is fairly large, it does not seriously affect the conclusions derived from the experimental data.

The results of experiments indicate that the diffusion porosity is on the order of 10^{-3} to 10^{-4} (fig. 4). Furthermore, the diffusion porosity is

a very small fraction of the total rock porosity, since $\phi'_D \approx 0.04\ \phi_T$ (fig. 5). Total rock porosities in the samples studied amount to 10^{-2} to 2×10^{-1} (fig. 6).

Of all the rocks examined during this study (tables 2 and 3), the volcanic rocks have the largest total porosities, from 0.2 to 2×10^{-1}, and ϕ'_D values, from 10^{-2} to 10^{-3} (figs. 4 and 6). Carbonate rocks studied have a fairly narrow range of total porosity values, from about 5×10^{-2} to less than 10^{-2}, whereas the ϕ'_D values range from 10^{-3} to 10^{-4}. The

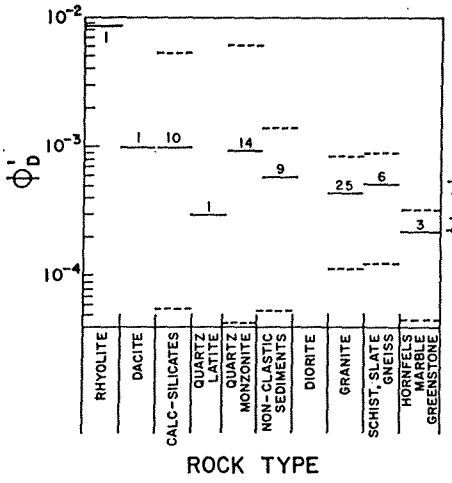

Fig. 4

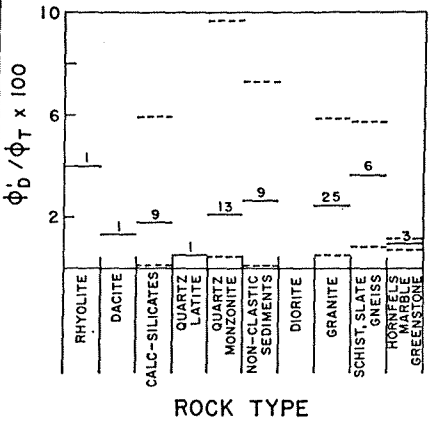

Fig. 5

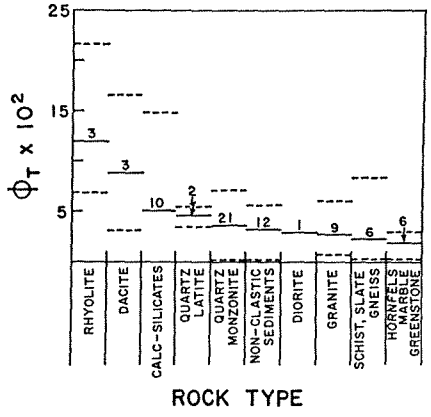

Fig. 6

Fig. 4. Mean values, solid lines, and range of values, dashed lines, of ϕ'_D for the various rock types examined in this study. The numerals denote the number of determinations for each rock type.

Fig. 5. The percentage of the total porosity that is composed of ϕ'_D. The solid lines are mean values, and the dashed lines are the range in values. The numerals denote the number of determinations for each rock type.

Fig. 6. Total porosity values for the various rock types studied. The solid lines are mean values, and the dashed lines the range in values. The numerals denote the number of determinations for each rock type.

TABLE 2

Density and porosity data

Sample no.	Bulk density ρ_B (g/cm^3)	Grain density ρ_γ (g/cm^3)	Total porosity $\phi_T \times 10^2$	$\phi'_D \times 10^4$	Sample thickness (cm)
Johnson Camp, Ariz.					
BQZ-5	2.61	2.72	4.11	8.1*	1.04
				13.7**	1.04
AL-007	2.68	2.74	2.12	5.5**	0.424
				1.5*	0.988
LA5	2.55	3.00	14.7	10.	0.90
AM-005	2.71	2.79	2.72	14.**	0.843
				2.*	0.800
AU-004	2.62	2.68	2.53		
ML-002	2.78	2.85	2.35		
MM-6	2.55	2.65	3.88		
MU-001	2.55	2.69	5.35		
ESC-3	2.64	2.71	2.62		
BP-4	2.60	2.70	3.85		
PS-1-JC	2.69	2.73	1.54	8.86**	0.925
				4.92*	0.964
Globe-Miami, Ariz.					
PS-1-GM	2.74	2.78	1.30		
Ronda, Spain					
R-71	2.74	2.76	.73	2.4*	0.386
R-80	2.77	2.80	1.07	3.3*	1.224
R-81	2.85	2.89	1.38	59.	1.29
R-125	2.72	2.97	8.42	7.1**	0.673
R-217	2.69	2.77	2.89	3.2	0.880
R-245	3.01	3.03	.660	3.7**	0.831
R-278	2.66	2.73	2.56	2.9	1.14
Chino, N.M.					
CS-1	2.69	2.97	9.43	7.5	1.05
CS-2	2.79	3.01	7.31	3.5	0.942
CS-4	2.75	2.83	2.83		
CS-5	4.25	4.67	8.99	53.	0.881
CS-6	3.01	3.12	3.53	9.7	1.33
CS-7	2.73	2.75	.73		
CS-8	3.18	3.24	1.85	7.0	1.19
CS-9	2.73	2.80	2.50	2.6	1.25
CS-10	2.72	2.73	.366	2.9	0.820
CS-11	2.64	2.71	2.58	4.1	1.02
CS-12	2.62	2.74	4.38	0.53	0.742
CS-13	2.49	2.67	6.74		
Chino pluton	2.62	2.69	2.60	10.	0.839
Silver City, N.M.					
Chino pc	2.97	2.99	.669	0.45	0.979
Cont. pit	2.91	3.03	3.96	0.54	0.949
150 pit	3.62	3.82	5.24	2.0	1.04
Copper Flat Pluton	2.48	2.62	5.34	2.9	0.857
San Manuel, Ariz.					
SM-1	2.71	2.75	1.46	1.1	1.04
SM-2	2.70	2.75	1.82	2.1	0.968
SM-3	2.71	2.87	5.58	4.1	1.02
SM-5	2.63	2.70	2.59	0.42	0.881
SM-7	2.45	2.63	6.84	11.	0.999
SM-8	2.57	2.70	4.82	8.8	0.958
SM-9	2.58	2.73	5.50	5.8	1.05

TABLE 2 (continued)

Sample no.	Bulk density ρ_B (g/cm^3)	Grain density ρ_Y (g/cm^3)	Total porosity $\phi_T \times 10^2$	$\phi'_D \times 10^4$	Sample thickness (cm)
Butte, Mont.					
8	2.73	2.91	6.35	61.	1.03
9A	3.04	3.22	5.41		
10282-2	2.60	2.71	3.77	8.4	1.18
10282-1	2.65	2.66	.0753	8.0	1.52
1024-1	2.74	2.77	1.55		
10283-1	2.73	2.76	1.01	2.4	1.12
Sierrita-Esperanza, Ariz.					
E-1	2.53	2.60	2.96		
E-2	2.66	2.71	1.96		
E-5	2.44	2.63	7.48		
ST-1	2.57	2.64	2.50		
ST-3	2.79	2.86	2.90		
ST-6	2.64	2.70	2.63	3.4	0.807
				1.1	1.27
Schultze Pluton, Globe-Miami, Ariz.					
S1 BB	2.51	2.65	5.35	3.9	0.840
SPV	2.61	2.66	1.77	4.8	1.0
				2.2	1.0
				8.3	0.507
SD5				16.0	0.144
				6.8	0.222
				6.1	0.280
5CM				5.2	0.481
3A				5.4	0.643
7CM				5.1	0.708
2				2.1	0.911
3				6.4	0.987
4				4.6	1.107
Bingham, Utah					
BGP	2.46	2.62	6.11	3.0	1.19
BQLP	2.58	2.65	2.64		
BWR	2.44	2.79	12.5	3.2	1.17
Miscellaneous					
SG-1	2.52	2.62	4.12		
LG-1	2.65	2.68	1.08	3.1	1.0
				2.0	1.0
RM-1	2.16	2.75	21.5	86.	0.888
TC-1	2.56	2.64	2.96		
AG-1	2.60	2.62	.611		
TR-3	2.62	2.65	1.36		
TR-5	2.46	2.66	7.52	9.9	1.09
TR-6	1.68	2.76	3.08		
DAC	2.20	2.61	15.7		

* Oriented perpendicular to foliation or bedding.
** Oriented parallel to foliation or bedding.

TABLE 3

Mineralogy of samples

Sample no.	Rock name	Mineralogy
Johnson Camp, Ariz.		
BQZ-5	Bolsa quartzite	quartz
AL-007	Lower Abrigo shale	clay, calcite
LA5	Lower Abrigo skarn	tremolite, muscovite, quartz, magnetite, hematite
AM-005	Middle Abrigo limestone	calcite, chert
AU-004	Upper Abrigo quartzite	quartz
AU-006	Upper Abrigo limestone	calcite, chert
ML-002	Lower Martin limestone	calcite
MM-6	Middle Martin limestone	calcite
MU-001	Upper Martin quartzite	quartz
ESC-3	Escabrosa marble	calcite
BP-4	Black Prince limestone	calcite
PS-1-JC	Pinal Schist	
Globe-Miami, Ariz.		
PS-1-GM	Pinal Schist	
Ronda, Spain		
R-71	slate	
R-80	biotite-garnet metapelite	andalusite, quartz, sericite, biotite, magnetite
R-81	quartzite	quartz, diopside, biotite, sphene, plagioclase, chlorite
R-125	pelitic schist	muscovite, tourmaline, andalusite, staurolite, quartz, biotite, garnet, plagioclase
R-217	hornfels	quartz, biotite, plagioclase, perthite, cordierite
R-245	granulite-grade gneiss	quartz, garnet, microperthite, plagioclase, sillimanite, biotite
R-278	hornfels	quartz, perthite, cordierite, plagioclase, biotite, sillimanite
Chino, N. Mex.		
CS-1	skarn	quartz, magnetite, pyrite, chalcopyrite
CS-2	skarn	quartz, sericite(?), biotite, magnetite, chlorite, pyrite, chalcopyrite
CS-3	skarn	quartz, andradite, magnetite, calcite, pyrite, chalcopyrite
CS-4	skarn	quartz, tremolite, magnetite, pyrite
CS-5	skarn	magnetite, quartz, pyrite, calcite
CS-6	skarn	amorphous silica, hematite, magnetite, calcite
CS-8	skarn	diopside, quartz, amorphous silica(?), calcite, magnetite
CS-9	skarn	quartz, calcite, diopside(?)
CS-10	Syrena limestone	calcite
CS-11	Upper Oswaldo limestone	calcite, quartz
CS-12	Lower Syrena limestone	calcite, quartz
CS-13	rhyolite subvolcanic	
Chino pluton	altered quartz monzonite porphyry	
Silver City, N. Mex.		
Chino pc	greenstone	
Cont. pit	skarn	quartz, andradite, magnetite, talc, sericite(?), pyrite, chalcopyrite, calcite
150 pit	skarn	andradite, quartz
Copper Flat pluton	quartz latite porphyry	

TABLE 3 (continued)

Sample no.	Rock name	Mineralogy
San Manuel, Ariz.		
SM-1	porphyritic Oracle quartz monzonite, altered	quartz, microcline, chlorite, biotite, plagioclase, hornblende, montmorillonite, epidote, hematite
SM-2	porphyritic Oracle quartz monzonite, altered	quartz, K-feldspar, plagioclase, chlorite, biotite, kaolinite, montmorillonite
SM-3	porphyritic Oracle quartz monzonite, altered	quartz, K-feldspar, sericite, kaolinite, biotite, plagioclase, pyrite, chlacopyrite, hematite
SM-5	porphyritic Oracle quartz monzonite, altered	quartz, K-feldspar, chlorite, plagioclase, sericite, pyrite, hematite, epidote
SM-7	quartz monzonite porphyry, altered	quartz, K-feldspar, plagioclase, chlorite, biotite, sericite, pyrite
SM-8	quartz monzonite porphyry, altered	quartz, sericite, chlorite, K-feldspar
SM-9	porphyritic Oracle quartz monzonite, altered	quartz, sericite, clay, plagioclase, microcline
Butte, Mont.		
8	sericitized Butte quartz monzonite	
9A	sericitized Butte quartz monzonite	with pyrite, chalcocite, enargite in vein
10282-2	argillized (white) Butte quartz monzonite	
10282-1	argillized (green) Butte quartz monzonite	quartz, potassium feldspar, plagioclase, biotite, hornblende, anhydrite
1024-1	altered Butte quartz monzonite	
10283-1	fresh Butte quartz monzonite	
Sierrita-Esperanza, Ariz.		
E-1	altered Esperanza quartz monzonite porphyry	quartz, plagioclase, K-feldspar, biotite, sericite, rutile, molybdenite, chalcopyrite
E-2	altered Esperanza quartz monzonite porphyry	quartz, plagioclase, K-feldspar, biotite, montmorillonite, pyrite, chalcopyrite, molybdenite
E-5	altered rhyolite	with quartz, hematite, sericite, pyrite
ST-1	altered quartz monzonite porphyry	quartz, K-feldspar, kaolinite, biotite, pyrite, chalcopyrite
ST-3	altered biotite quartz diorite	plagioclase, biotite, montmorillonite(?), chlorite, sericite, epidote, quartz
ST-6	altered Harris Ranch quartz monzonite	quartz, plagioclase, K-feldspar, hornblende, kaolinite, chlorite, biotite, calcite, pyrite, hematite
Schultze Pluton, Globe-Miami, Ariz.		
S1 BB	altered porphyritic Schultze Granite	quartz, K-feldspar, plagioclase, biotite, clays, muscovite, calcite, Cu oxides
SPV	equigranular Schultze Granite	quartz, K-feldspar, plagioclase, biotite, kaolinite, muscovite, clays

TABLE 3 (continued)

Sample no.	Rock name	Mineralogy
Porphyritic Schultze Granite, Globe-Miami, Ariz.		
SD5	porphyritic granite	
SD5	porphyritic granite	
SD5	porphyritic granite	
5CM	porphyritic granite	
3A	porphyritic granite	
7CM	porphyritic granite	
2	porphyritic granite	
3	porphyritic granite	
4	porphyritic granite	
Bingham, Utah		
BGP	Bingham granite porphyry	
BQLP	Bingham quartz latite porphyry	
BWR	Bingham latite dike	
Miscellaneous		
SG-1	Stronghold granite (Cochise's Stronghold, Ariz.)	
LG-1	Sherman granite (Laramie, Wyo.)	
RM-1	altered tuff (Red Mountain, Ariz.)	
TC-1	Texas Canyon granite (Texas Canyon, Ariz.)	quartz, K-feldspar, plagioclase, biotite, muscovite
AG-1	Amole granite (Tucson, Ariz.)	
TR-3	Troy granite (Troy, Ariz.)	
TR-5	rhyodacite dike (Troy, Ariz.)	
TR-6	dacite dike (Troy, Ariz.)	
DAC	dacite flow (Superior, Ariz.)	

plutonic rocks studied have a very uniform total porosity, with all values falling within several units of 4×10^{-2}. But, similar to the carbonate rocks, ϕ'_D varies greatly, between about 5×10^{-3} and 4×10^{-5}. The calc-silicate altered rocks have large values of both total and diffusion porosity, with ϕ_T between 1.5×10^{-1} and 3×10^{-3} and ϕ'_D between about 5×10^{-3} and 5×10^{-5}.

Many of the hydrothermally altered calc-silicate and plutonic rocks have significantly greater values for both total porosity and ϕ'_D than their unaltered equivalents (tables 2 and 3). The mean total porosity for the calc-silicates from Chino, N. M. is 4.6×10^{-2}, compared to 2.4×10^{-2} for their unaltered equivalents, and the mean ϕ'_D for these same rocks is $1.2\ 10^{-3}$ as compared to $2.4\ 10^{-4}$ for the unaltered equivalents. The altered rocks from Butte, Mont. also show this trend; the mean total porosity is 3.2×10^{-2}, compared to 1.1×10^{-2}, respectively, and the mean ϕ'_D is 2.6×10^{-3}, compared to 2.4×10^{-4} for unaltered equivalents.

Comparison of the hydrothermally altered plutonic rocks from San Manuel and Sierrita-Esperanza, Ariz. with unaltered rocks from the Laramie, Wyoming and Troy, Ariz. plutons suggests a similar result, although samples SM-5, with $\phi'_D = 4.2 \times 10^{-5}$, (San Manuel, Ariz.), and CS-7 (Chino, N.M.), with $\phi_T = 7.3 \times 10^{-3}$, deviate significantly from this trend. It is interesting to note that the bulk of the difference in pore volume between hydrothermally altered rocks and their unaltered equivalents is due to a markedly larger value of residual porosity in the altered rocks (table 2). Since the mineral surface area:fluid ratio is very large, porosity increase due to irreversible chemical mass transfer in the residual pores is negligible; this larger value must be a result of either initial condition or subsequent modification of the initial porosity.

Total porosities for the isotropic metamorphic rocks studied range from about 3×10^{-2} to less than 10^{-2}; ϕ'_D for these same rocks varies from about $3.0\ 10^{-4}$ to about $4.5\ 10^{-5}$. The anisotropic rocks studied have a wider range in total porosity, with values ranging from about 10^{-1} to less than 10^{-2} (table 4). These values show that ϕ'_D parallel to foliation or bedding is significantly greater than that perpendicular, by a factor of about 2 to 7.

A consistent ratio between ϕ'_D and total porosity, that is, 4×10^{-2}, is also apparent in the data. This consistency suggests that ϕ'_D can be estimated from rather simple measurements of ϕ_T.

The total diffusion porosity, ϕ_D, may be computed from values of ϕ'_D determined above, eq (22), and the transient times required to attain steady state in the experiments. Values for an altered quartz monzonite, SM7, and a metapelite, 80, indicate that ϕ'_D is simply one axial component of ϕ_D, that is, $\phi_D = 3\phi'_D$.

RESIDUAL POROSITY

Residual porosity, ϕ_R, is the bulk of the total rock porosity since the analysis of the flow and diffusion porosity indicates that the sum of ϕ_F and ϕ_D amounts to a small fraction of the total porosity, for example, 10^{-1}. Therefore, residual porosity is $> 0.9\ \phi_T$ in fractured media.

NATURE OF PORES

Location, relative size distribution, and continuity of the pores can be determined by an analysis of porosity and mineral size distributions (figs. 7 and 8) and direct observation. The porosity distribution, exclusive of flow porosity, is obtained by measuring the density as a function

TABLE 4

Values for ϕ'_D by orientation of sample

Sample	Parallel	Perpendicular
AL007	5.40×10^{-4}	1.48×10^{-4}
AM005	13.9	2.01
PS-1-JC	8.86	4.92
BQZ	13.7	8.05

of crushed grain size. Intergranular porosity requires the density of the crushed aggregate and, hence, total measured porosity to increase as the size of the crushed grains decreases. As the crushed-grain size approaches a mineral-grain size a greater increase is expected. The contributions to porosity from pores around grains of various sizes can be calculated by using the density of the smallest grain in the interval as ρ_γ in eq 2. Measurements of this type were made on samples of the equigranular and porphyritic Schultze Granite (figs. 7 and 8).

The correlation between mineral grain size and porosity distributions for the porphyritic Schultz Granite (fig. 7) indicates the pores occur between grains and that pore size is bimodally distributed. Mode I is composed almost wholly of pores with a maximum dimension greater than 4 mm, constituting 30 percent of the total pore volume. Mode II is composed of pores that have a maximum dimension less than 1 mm, constituting 70 percent of the pore volume. In mode I there is a large increase in pore volume (30 percent), as the crushed grain size approaches 4 mm. Because this size interval corresponds to the phenocryst size range, it can be concluded that this pore volume is located around the phenocrysts. The imperfect correlation between grain size and porosity in the size interval, 4 to 1 mm, can be interpreted to mean that there is very little pore volume located around the minerals in this size interval. Finally, the porosity distribution volume in mode II roughly mimics

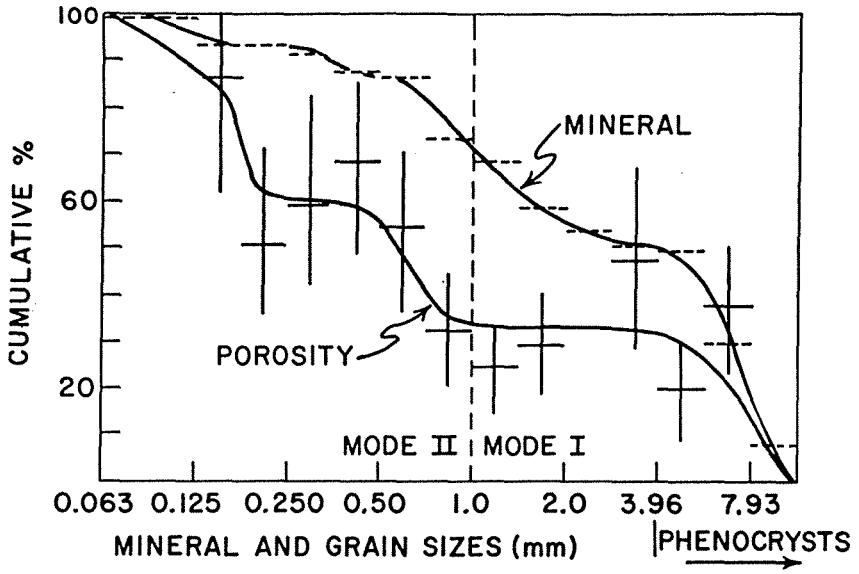

Fig. 7. Measurements of porphyritic Schultze Granite showing cumulative percentage of porosity as a function of crushed grain sizes. Horizontal bars are plotted at actual measured porosity values, with their length representing the precision of the crushed grain size measurement. Vertical bars represent the precision of the porosity measurement, also, cumulative percentage mineral sizes as a function of mineral size. Horizontal dashed lines represent precision for the size ranges.

the mineral distribution, again indicating that these pores are located around these minerals.

The intergranular nature of the pores implies that they have a maximum dimension less than or equal to their associated mineral dimension; that is, the more continuous pores are located around the larger mineral sizes. The porosity and mineral size distribution curves in mode I also indicate that 30 percent of the pore volume is located around the larger minerals, which at the most comprise 50 percent of the mineral surface area in the rock, whereas in mode II 70 percent of the pore volume is located around 30 percent of the minerals.

The porosity and mineral distribution for the equigranular Schultze Granite also shows there is one domain of porosity closely correlated with mineral distribution (fig. 8). The lack of correlation in mode I, however, permits two conclusions about pore location and continuity. The larger pores are either intergranular and less than or equal to the mineral dimensions or elongate pores that crosscut mineral boundaries.

The continuity of intergranular pores in the porphyritic Schultze Granite can be determined from ϕ'_D values for samples of varying thicknesses (fig. 9). Large increases in ϕ'_D indicate large abundances of pores with a maximum dimension equal to that sample thickness. These data indicate a discontinuity at about 8 mm, which is also suggested by correlative changes of porosity and mineral abundance distribution

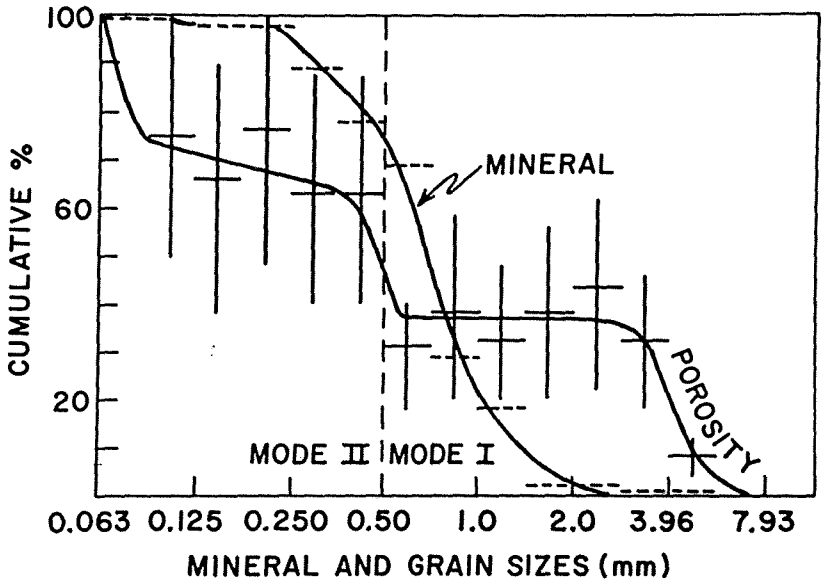

Fig. 8. Measurements on equigranular Schultze Granite showing cumulative percentage of porosity as a function of crushed grain sizes. Horizontal bars are plotted at actual measured porosity values, with their length representing the precision of the crushed grain size measurement. Vertical bars represent the precision of the porosity measurement, also, cumulative percentage mineral sizes as a function of mineral size. Horizontal dashed lines represent precision for the size ranges.

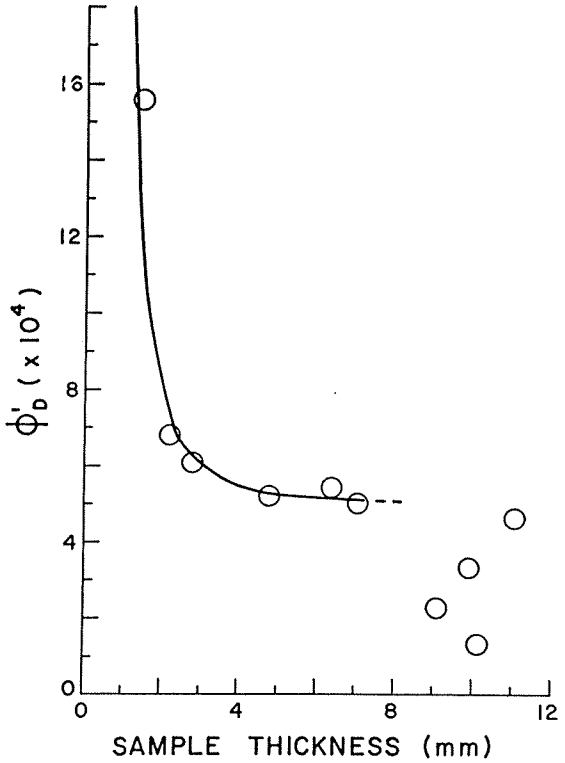

Fig. 9. Variation of ϕ'_D with the thickness of the porphyritic Schultze Granite samples used in diffusion experiment.

curves in mode I (fig. 7). This discontinuity indicates that there is a large abundance of pores with a maximum dimension of about 8 mm and that these more continuous pores are located around the phenocrysts.

The large increase in ϕ'_D at about 2 mm (fig. 9) indicates that the preponderance of pores have a maximum dimension less than this length. This increase of ϕ'_D approaches the value of the total porosity as the sample thickness approaches zero. Previous experiments determined (Garrels, Dreyer, and Howland, 1949) that $\phi'_D/\phi_T = 0.4$ for limestone samples 1 to 2 mm thick. These values are in general agreement with those reported in our study, if one assumes the relationship in figure 9 holds for a variety of rock types.

The geometry of discontinuous pores in fractured media may be classified into two broad categories, equidimensional pores and microcracks. Equidimensional pores vary from less than 1 mm to as great as 5 mm. This upper limit in size for equidimensional pores coincides with the large increase in the porosity distributions (figs. 7 and 8) and serves as partial confirmation of these curves. The pores composing this category have shapes that range from prismatic to highly irregular. Observed apertures of the microcracks range from less than 1 μm to no

PLATE 2

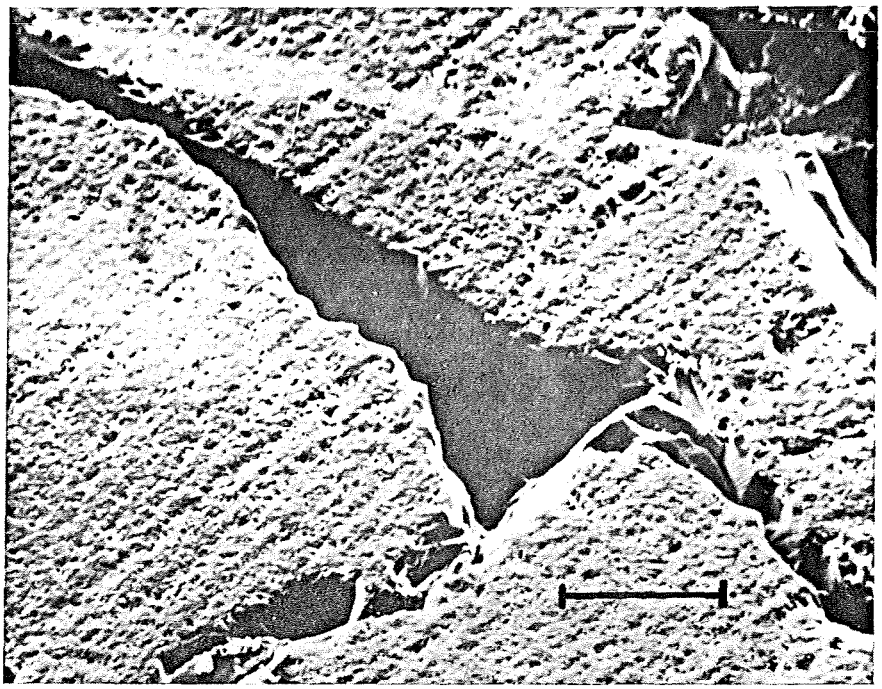

Scanning electron micrograph of an intergranular-prismatic pore in the Sherman Granite. This type of pore probably represents the geometry and size of diffusion and/or residual pores. The scale bar is 100 μm.

greater than 40 μm. Clearly, the small values for the apertures require the bulk of the pore volume to be composed of equidimensional pores. The suggested intergranular nature of the pores is also supported by the above observations, since the equidimensional pores are clearly distributed around grain boundaries (pl. 2).

In summary, the above data suggest that a general porosity model for fractured igneous rocks consists of continuous planar fractures, ϕ_F, and cylindrical pores, ϕ_D (fig. 10).

ADVECTION–REACTION–DIFFUSION

Porosity data define the distribution of fluids in hydrothermal systems. This information permits formulation of the governing partial differential equations for the advection-diffusion-reaction of aqueous species in a hydrothermal system.

The actual paths described by circulating packets of fluid in and around cooling intrusive bodies are defined in two dimensions by

$$\frac{dx}{\bar{v}_x} = \frac{dz}{\bar{v}_z} = dt, \tag{23}$$

where $\bar{v}_x$ and $\bar{v}_z$ are the component velocities. Examples of these pathlines in hydrothermal systems are presented in Norton and Knight, 1977. Fluids circulating along pathlines flow from one chemical environment into another, which results in differences in fluid compositions between those fluids in the flow porosity and those in the diffusion porosity, as well as disequilibrium between fluids and mineral phases. The transfer of heat between circulating fluid and rock may cause further disequilibrium within a rock volume. The mass transfer resulting from this disequilibrium occurs within flow porosity and diffusion porosity.

Advective transport depends directly on the magnitude of the flow velocities in ϕ_F. For flow velocities normally realized in these systems, a parabolic flow profile develops in less than a meter along the fracture and is effective over a thickness equal to half the fracture aperture (fig. 10). The true velocity in the fracture varies from zero at the wall of the fracture to an average value, defined by

$$\bar{v}_t = \frac{\bar{v}_{Darcy}}{\phi_{flow}}. \tag{24}$$

Therefore, the advective flux of the i^{th} ion is

$$\bar{u}_i = \bar{v}_t m_i \phi_F \rho. \tag{25}$$

The diffusional flux within ϕ_F parallel to the flow direction and across a concentration boundary layer, δ_c, follows from eq (17) with the substitution of ϕ_F for ϕ_D.

$$\bar{u}_{iF} = -\phi_F \sum_k D_{ik} \nabla_{xy} m_k. \tag{26}$$

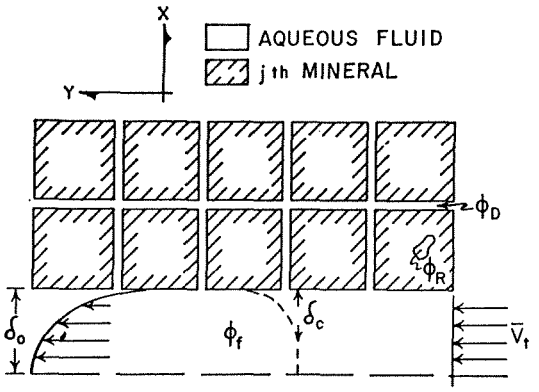

Fig. 10. Schematic two-dimensional porosity model for homogenous and isotropic ϕ_D. The model represents a possible geometric distribution of pores with respect to discrete minerals and is consistent with data collected in this study. In particular, we note that diffusion pores, ϕ_D, occur along each mineral grain boundary and interconnect with continuous fractures, ϕ_F. Although the relative abundance of the porosity types is not represented in this schematic representation, typical values for the porosity parameter are $\phi_D = 2 \times 10^{-4}$, $\phi'_D = 3\phi_D$, $\tau = 1$, diffusion pore radius of 10^{-3} cm and mineral sizes of 0.14 cm. The model and values are a first order approximation of pore geometry in fractured rocks.

As discussed previously, aqueous diffusion is the dominant transport mechanism within the diffusion pores and is defined by

$$\bar{u}_{iD} = -\phi'_D \sum_k D_{ik} \nabla_{xy} m_k. \tag{27}$$

The total flux of the i^{th} ion from the representative region, R, can be obtained by summing the advective and diffusive fluxes within the flow porosity domain and the diffusive flux within the diffusion porosity domain (eqs 25, 26, and 27).

$$\bar{S}_i = \bar{u}_i + \bar{u}_{iF} + \bar{u}_{iD}. \tag{28}$$

An expression for the total amount of the i^{th} ion in R available for transport can be obtained by modifying eq (19) to read

$$M_i = \int_R \rho (\phi_F + \phi_D) (m_i + A_i m_i) \, dV. \tag{29}$$

The amount of the i^{th} ion loss from R is equal to the volume integral of the divergence of $\bar{S}_i$,

$$-\int_R \operatorname{div} \bar{S}_i \, dV, \tag{30}$$

and must be equal to the rate of depletion of the ion in R, that is, the time derivative of eq (29). Introducing a conservation of mass and combining the time derivative of eqs (29) and (30) results in the governing partial differential equation for conservation of the i^{th} aqueous species:

$$\rho (\phi_F + \phi_D) (A_i + 1) \frac{\partial m_i}{\partial t} + \rho \bar{v}_t \phi_F \nabla m_i = \nabla D_{ik} \phi_F \nabla m_k + \nabla D_{ik} \phi'_D \nabla m_k. \tag{31}$$

Eq (31), together with the partial differential equations describing fluid flow in pluton environments, accounts for the circulation of fluids through reactive host rocks. This formulation is fundamentally different from previously derived equations in that it explicitly affords for the appropriate porosity values in fractured rocks. Other formulations utilize total rock porosity, which may produce significantly different results since we found ϕ_T is as large as several orders of magnitude greater than $(\phi_D + \phi_F)$.

ACKNOWLEDGMENTS

This research was supported by NSF Grant nos. GA-41136 and EAR74-03515-A01 and the University of Arizona. We wish to thank Dr. Timothy Loomis, Mr. Bill Baltosser, Bear Creek Mining Company, the University of Arizona chapter of SGE, and the Anaconda Company for donating samples and rock descriptions which greatly enhanced the scope of this study. We also wish to thank Lynn McLean for improvements in the manuscript.

REFERENCES

Bianchi, L., and Snow, D. T., 1969, Permeability of crystalline rocks interpreted from measured orientations and apertures of fractures: Jodphur, Rajasthan, Arid Zone Research Assoc. of India, Annals of Arid Zone, v. 8, no. 2, p. 231-245.

Boardman, C. R., and Skrove, J., 1966, Distribution in fracture permeability of a granitic rock mass following a contained nuclear explosion: Jour. Petroleum Technology, v. 18, p. 619-623.

Brace, W. F., Walsh, J. B., and Frangos, W. T., 1968, Permeability of granite under high pressure: Jour. Geophys. Research, v. 73, p. 2225-2236.

Brace, W. F., 1971, Resistivity of saturated crustal rocks to 40 km based on laboratory measurements, *in* Heacock, J. G., ed., The structure and physical properties of the Earth's crust: Am. Geophys. Union, Geophys. Mon. Ser., v. 14, p. 243-255.

Cadek, J., Hazdrova, M., Kacura, G., Krasny, J., and Malkovsky, M., 1968, Hydrogeology of the thermal waters at Teplice and Usti nad Labem: Sbornik Geol. Ved, Hydrogeol., Inzenyrska Geol., rada HIG, sv. 6, p. 1-184.

Davis, S. N., 1969, Porosity and permeability of natural materials, *in* DeWiest, R. J. M., ed., Flow through porous media: New York, Acad. Press, p. 54-90.

DeWiest, R. J. M., 1965, Geohydrology: New York, John Wiley & Sons, Inc., 366 p.

Fatt, I., 1956, The network model of porous media: Am. Inst. Mining Engineers, Petroleum Trans., v. 207, p. 141-181.

Garrels, R. M., Dreyer, Z. M., and Howland, D. L., 1949, Diffusion of ions through intergranular spaces in water saturated rocks: Geol. Soc. America Bull., v. 60, p. 1809-1828.

Grindley, G. W., 1965, The geology, structure, and exploitation of the Wairakei geothermal field: Taupo, New Zealand: Wellington, New Zealand Geol. Survey, 131 p.

Hubbert, M. K., 1940, The theory of ground-water motion: Jour. Geology, v. 48, p. 785-944.

Jackson, D. B., 1966, Deep resistivity probes in the southwestern United States: Geophysics, v. 31, p. 1123-1144.

Keller, G. V., Anderson, L. A., and Pritchard, J. I., 1966, Geological survey investigations of the electrical properties of the crust and upper mantle: Geophysics, v. 31, p. 1078-1087.

Knapp, R. B., ms, 1975, An analysis of the porosities of fractured crystalline rocks: M.S. thesis, Univ. Arizona, 90 p.

Maini, Y. N. T., ms., 1971, In situ hydraulic parameters in jointed rock—their measurement and interpretation: Ph.D. dissert., Univ. London, 312 p.

Marine, I. W., 1966, Hydraulic correlation of fracture zones in buried crystalline rock at the Savannah River plant, near Aiken, South Carolina: U.S. Geol. Survey Prof. Paper 550-D, p. 223-227.

Norton, D. L., and Knight, J. E., 1977, Transport phenomena in hydrothermal systems: cooling plutons: Am. Jour. Sci., v. 277, p. 937-981.

Ohle, E. L., 1951, The influence of permeability on ore distribution in limestone and dolomite: Econ. Geology, v. 46, p. 667-706.

Plauff, D., 1966, Magneto-telluric soundings in the southwestern United States: Geophysics, v. 31, p. 1145-1152.

Pratt, H. R., Black, A. D., Brace, W. F., and Norton, D. L., 1974, In situ joint permeability in a granite: EOS, Am. Geophys. Union Trans., v. 55, p. 433.

Snow, D. T., ms, 1965, A parallel plate model of fractured permeable media: Ph.D. dissert., Univ. California, Berkeley, 331 p.

———— 1970, The frequency and apertures of fractures in rock: Internat. Jour. Rock Mechanics Min. Sci., v. 7, p. 23-40.

Villas, R. N., ms., 1975, Fracture analysis, hydrodynamic properties and mineral abundance in altered igneous wall rocks of the Mayflower mine, Park City district, Utah: Ph.D. dissert., Univ. Utah, Salt Lake City, 253 p.

Winograd, I. J., 1971, Hydrogeology of ash flow tuff: a preliminary statement: Water Resources Research, v. 7, p. 994-1006.